

International Journal of Physical Sciences

Volume 9 Number 20 30 October, 2014

ISSN 1992-1950



*Academic
Journals*

ABOUT IJPS

The **International Journal of Physical Sciences (IJPS)** is published weekly (one volume per year) by Academic Journals.

International Journal of Physical Sciences (IJPS) is an open access journal that publishes high-quality solicited and unsolicited articles, in English, in all Physics and chemistry including artificial intelligence, neural processing, nuclear and particle physics, geophysics, physics in medicine and biology, plasma physics, semiconductor science and technology, wireless and optical communications, materials science, energy and fuels, environmental science and technology, combinatorial chemistry, natural products, molecular therapeutics, geochemistry, cement and concrete research, metallurgy, crystallography and computer-aided materials design. All articles published in IJPS are peer-reviewed.

Contact Us

Editorial Office: ijps@academicjournals.org

Help Desk: helpdesk@academicjournals.org

Website: <http://www.academicjournals.org/journal/IJPS>

Submit manuscript online <http://ms.academicjournals.me/>

Editors

Prof. Sanjay Misra

*Department of Computer Engineering, School of Information and Communication Technology
Federal University of Technology, Minna,
Nigeria.*

Prof. Songjun Li

*School of Materials Science and Engineering,
Jiangsu University,
Zhenjiang,
China*

Dr. G. Suresh Kumar

*Senior Scientist and Head Biophysical Chemistry
Division Indian Institute of Chemical Biology
(IICB)(CSIR, Govt. of India),
Kolkata 700 032,
INDIA.*

Dr. Remi Adewumi Oluyinka

*Senior Lecturer,
School of Computer Science
Westville Campus
University of KwaZulu-Natal
Private Bag X54001
Durban 4000
South Africa.*

Prof. Hyo Choi

*Graduate School
Gangneung-Wonju National University
Gangneung,
Gangwondo 210-702, Korea*

Prof. Kui Yu Zhang

*Laboratoire de Microscopies et d'Etude de
Nanostructures (LMEN)
Département de Physique, Université de Reims,
B.P. 1039. 51687,
Reims cedex,
France.*

Prof. R. Vittal

*Research Professor,
Department of Chemistry and Molecular
Engineering
Korea University, Seoul 136-701,
Korea.*

Prof Mohamed Bououdina

*Director of the Nanotechnology Centre
University of Bahrain
PO Box 32038,
Kingdom of Bahrain*

Prof. Geoffrey Mitchell

*School of Mathematics,
Meteorology and Physics
Centre for Advanced Microscopy
University of Reading Whiteknights,
Reading RG6 6AF
United Kingdom.*

Prof. Xiao-Li Yang

*School of Civil Engineering,
Central South University,
Hunan 410075,
China*

Dr. Sushil Kumar

*Geophysics Group,
Wadia Institute of Himalayan Geology,
P.B. No. 74 Dehra Dun - 248001(UC)
India.*

Prof. Suleyman KORKUT

*Duzce University
Faculty of Forestry
Department of Forest Industrial Engineering
Beciyorukler Campus 81620
Duzce-Turkey*

Prof. Nazmul Islam

*Department of Basic Sciences &
Humanities/Chemistry,
Techno Global-Balurghat, Mangalpur, Near District
Jail P.O: Beltalapak, P.S: Balurghat, Dist.: South
Dinajpur,
Pin: 733103,India.*

Prof. Dr. Ismail Musirin

*Centre for Electrical Power Engineering Studies
(CEPES), Faculty of Electrical Engineering, Universiti
Teknologi Mara,
40450 Shah Alam,
Selangor, Malaysia*

Prof. Mohamed A. Amr

*Nuclear Physic Department, Atomic Energy Authority
Cairo 13759,
Egypt.*

Dr. Armin Shams

*Artificial Intelligence Group,
Computer Science Department,
The University of Manchester.*

Editorial Board

Prof. Salah M. El-Sayed

*Mathematics. Department of Scientific Computing,
Faculty of Computers and Informatics,
Benha University. Benha ,
Egypt.*

Dr. Rowdra Ghatak

*Associate Professor
Electronics and Communication Engineering Dept.,
National Institute of Technology Durgapur
Durgapur West Bengal*

Prof. Fong-Gong Wu

*College of Planning and Design, National Cheng Kung
University
Taiwan*

Dr. Abha Mishra.

*Senior Research Specialist & Affiliated Faculty.
Thailand*

Dr. Madad Khan

*Head
Department of Mathematics
COMSATS University of Science and Technology
Abbottabad, Pakistan*

Prof. Yuan-Shyi Peter Chiu

*Department of Industrial Engineering & Management
Chaoyang University of Technology
Taichung, Taiwan*

Dr. M. R. Pahlavani,

*Head, Department of Nuclear physics,
Mazandaran University,
Babolsar-Iran*

Dr. Subir Das,

*Department of Applied Mathematics,
Institute of Technology, Banaras Hindu University,
Varanasi*

Dr. Anna Oleksy

*Department of Chemistry
University of Gothenburg
Gothenburg,
Sweden*

Prof. Gin-Rong Liu,

*Center for Space and Remote Sensing Research
National Central University, Chung-Li,
Taiwan 32001*

Prof. Mohammed H. T. Qari

*Department of Structural geology and remote sensing
Faculty of Earth Sciences
King Abdulaziz UniversityJeddah,
Saudi Arabia*

Dr. Jyhwen Wang,

*Department of Engineering Technology and Industrial
Distribution
Department of Mechanical Engineering
Texas A&M University
College Station,*

Prof. N. V. Sastry

*Department of Chemistry
Sardar Patel University
Vallabh Vidyanagar
Gujarat, India*

Dr. Edilson Ferneda

*Graduate Program on Knowledge Management and IT,
Catholic University of Brasilia,
Brazil*

Dr. F. H. Chang

*Department of Leisure, Recreation and Tourism
Management,
Tzu Hui Institute of Technology, Pingtung 926,
Taiwan (R.O.C.)*

Prof. Annapurna P.Patil,

*Department of Computer Science and Engineering,
M.S. Ramaiah Institute of Technology, Bangalore-54,
India.*

Dr. Ricardo Martinho

*Department of Informatics Engineering, School of
Technology and Management, Polytechnic Institute of
Leiria, Rua General Norton de Matos, Apartado 4133, 2411-
901 Leiria,
Portugal.*

Dr Driss Miloud

*University of mascara / Algeria
Laboratory of Sciences and Technology of Water
Faculty of Sciences and the Technology
Department of Science and Technology
Algeria*

ARTICLES

- | | |
|---|------------|
| Detection of energetic particles from plasma focus using Faraday cup and SSNTD (LR-115A) | 438 |
| G. M. El-Aragi | |
| Guiding of light with pinholes | 444 |
| Makoto Morinaga | |
| Chemical composition and antioxidant capacity of the leaf extract of <i>Justicia insularis</i> | 454 |
| O. T. Adeyemi and O. Babatunde | |

Full Length Research Paper

Detection of energetic particles from plasma focus using Faraday cup and SSNTD (LR-115A)

G. M. El-Aragi

Plasma Physics and Nuclear Fusion Department, Nuclear Research Center, AEA, P. O. Box 13759 Cairo, Egypt.

Received 26 August, 2014; Accepted 26 September, 2014

A Mather-type plasma focus device is used in this work which is prefilled with helium at 0.8 Torr. The total ion current density of the plasma stream is measured to be 750 mA/cm². From time-resolved measurements (Faraday cup), the ion beam energy was distributed with energy ranging from 0.3 to 540 keV. The ion flux density of ion beam is estimated to be 4.47×10^{11} ion/steradian using track etching technique (LR-115A).

Key words: Energetic ions, plasma focus, charging voltage.

INTRODUCTION

Ion diagnostics of high-temperature plasma objects are considered to be very important, because they provide essential data about plasma parameters. Ion beams emitted from the high-temperature plasma objects are an abundant source of valuable information about fusion reaction yields, plasma ion temperatures, as well as a spatial distribution of fusion reaction sources.

In several theoretical papers (Bernstein, 1970; Jager and Herold, 1987; Pasternak and Sadowski, 1998) very simple configurations have been adopted to explain ion behavior inside of the plasma column. Experimental studies of Dense Plasma Focus (DPF) facilities proved the occurrence of high-energy ion beams, generated within the plasma focus pinch column or its vicinity. High energetic ions are considered to play an important role in the production of the intense neutron flux in the plasma focus device when using deuterium gas (Zakaullah et al., 1999). Studies of high-energy ions emitted from plasma focus devices provide information on the ion acceleration

mechanisms and are also important for various plasma focus technology. Gerdin et al. (1981) employed a Faraday cup in a time-of-flight technique to measure the ion spectrum and a careful study of the ion-neutral interactions allowed the observation of deuteron energies down to ~ 25 keV. Different kinds of acceleration mechanisms for charge particle were identified (Mather, 1971; Deutsch and Kies, 1988). General characteristics of the ion beams were studied in different laboratories (Gerdin et al., 1981; Kelly and Marquez, 1996).

Track etching technique has been successfully employed in many insulating materials for detection and identification of charged particles, e.g. in the study of heavy primary cosmic rays, the search for super heavy elements and innumerable applications in radiation dosimeters.

Early in the past decade cellulose nitrate as recognized as the most sensitive of all track detectors, and so has been used as a detector to record protons.

E-mail: elaragi@yahoo.com

Author(s) agree that this article remain permanently open access under the terms of the [Creative Commons Attribution License 4.0 International License](https://creativecommons.org/licenses/by/4.0/)

PACS: 52.59.Hq

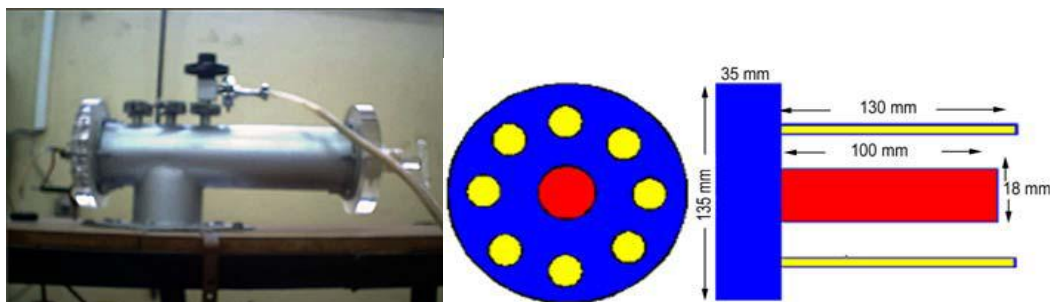


Figure 1. Schematic of experimental setup.

EXPERIMENTAL SETUP

Mather-type 112.5 J plasma focus device consists of an outer electrode, which is formed of eight copper rods, each of 130 mm length and 10 mm diameters as shown in Figure 1. The outer diameter of center electrode is 18 mm and inner diameter of squirrel cage (outer electrode) is 55 mm. A hole of 5 mm diameter and 8 mm depth was drilled in the front of the inner electrode in which different metals were filled. The cylindrical insulator ring is of 130 mm diameter and 35 mm thickness. The electrode system is enclosed in a vacuum chamber made of stainless steel tank of 350 mm length and 100 mm diameter. There are several ports in the vacuum chamber for diagnostic purposes. The condenser bank of plasma focus device consists of one condenser of 25 kV and 1 μ F low inductance condenser. A capacitor bank charged at 15 kV (112.5 J), giving peak discharge current of about 5 kA, powered the focus device. The inner electrode is connected to the positive connection of high voltage supply via a triggertron-type vacuum tube (CX1159) served as a switch, whereas the outer electrode is grounded.

The vacuum chamber was evacuated up to 10^{-2} mbar pressure by a rotary pump (Edwards single stage model 1 Sc.-150B) before filling gas (helium). To avoid vapor from back streaming, the vacuum chamber is washed by gas after evacuation by rotary pump. The gas was fed into the system via flow meter (OMEGA model). The external inductance of the system including the capacitor, thyatron switch, connecting cables and coaxial electrodes (cathode and anode) is measured to about 6.5 μ H.

In order to register the particle radiation within the pinhole camera, the use of nuclear track detectors of the LR-115A type was made. After irradiation those detectors were etched under standard conditions (in a 6.25-N solution of NaOH, at a temperature of 70°C) for a period ranging from one hour to several hours. To perform time-resolved measurements Faraday-type collectors were used: a single cup (FC) and a so-called double-cup system (DFC), which used two ring-shaped collectors placed at a given distance (time-of-flight basis), but adjusted along the common z-axis.

The applied voltage and the discharge current through the discharge chamber were measured using a voltage divider (Home made), which was connected between the two electrodes, and a current monitor, which can be located upon returning to the ground. The signals from the voltage divider and the current monitor were recorded in a digitizing oscilloscope (Lecroy, USA) with a 200-MHz bandwidth.

The peak value of the discharge current was measured approximately 5 kA during the pulse. Figure 2 shows the current and voltage waveforms that characterized the pulsed low energy plasma focus device. Current and voltage were measured as a function of time at an input energy of 112.5 J (maximum applied voltage 15 kV).

RESULTS AND DISCUSSION

The Plasma Focus (PF) is a device consisting in two coaxial electrodes in vacuum connected to a fast high voltage capacitor bank and separated by an insulator. When the high voltage (HV) is applied to the electrodes through a thyatron switch, an electrical breakdown develops on the surface of the insulator and the discharge is driven by the Lorentz force to run along the gap between the electrodes at a speed of some 10^6 cm/s and when reaches the end of the inner electrode collapses on the axis of the device focusing in a hot blob of plasma (Plasma Focus). In this phase strong electric fields are generated that produce intense ion beams. The duration of each discharge is of the order of 8 μ s.

Preliminary time-resolved measurements of the ion pulses were carried out by means of an ion collector, which was placed at a distance of 20 cm from the top of the anode. The ion collector consists of a copper disc of 2.0 cm diameter which is connected to the ground through resistor ($R = 75$ m Ω). The voltage develop across the resistor is fed it digital storage oscilloscope (Lecroy) to record the ion current signals. The collector plate was polarized negatively, and the whole measuring circuit was shielded against electromagnetic noise. Time-resolved studies of ions were performed by means of a double-collector of the Faraday type, which was designed especially for time of flight (TOF) measurements of pulsed charged-particle streams. That detector was equipped with two separate collectors (collector and grid) adjusted along the same Z-axis. The first ring-shaped collector (grid) was placed at a distance of 20 cm from the focus pinch, and the second one was situated about 2 cm behind the first collector. Some examples of the registered traces of the collector signals are presented in Figure 3. The velocity, energy and density of helium ions are estimated using TOF technique (Gerdin et al., 1981; Wong et al., 2002). The ion velocity is estimated by taking the ratio of the distance to the flight time of ions from source to detector (Lee and Saw, 2013). The variation of ion flux with filling helium gas pressure is shown in Figure 4. It is note that the maximum ion flux reaches at maximum value at pressure 0.8 Torr,

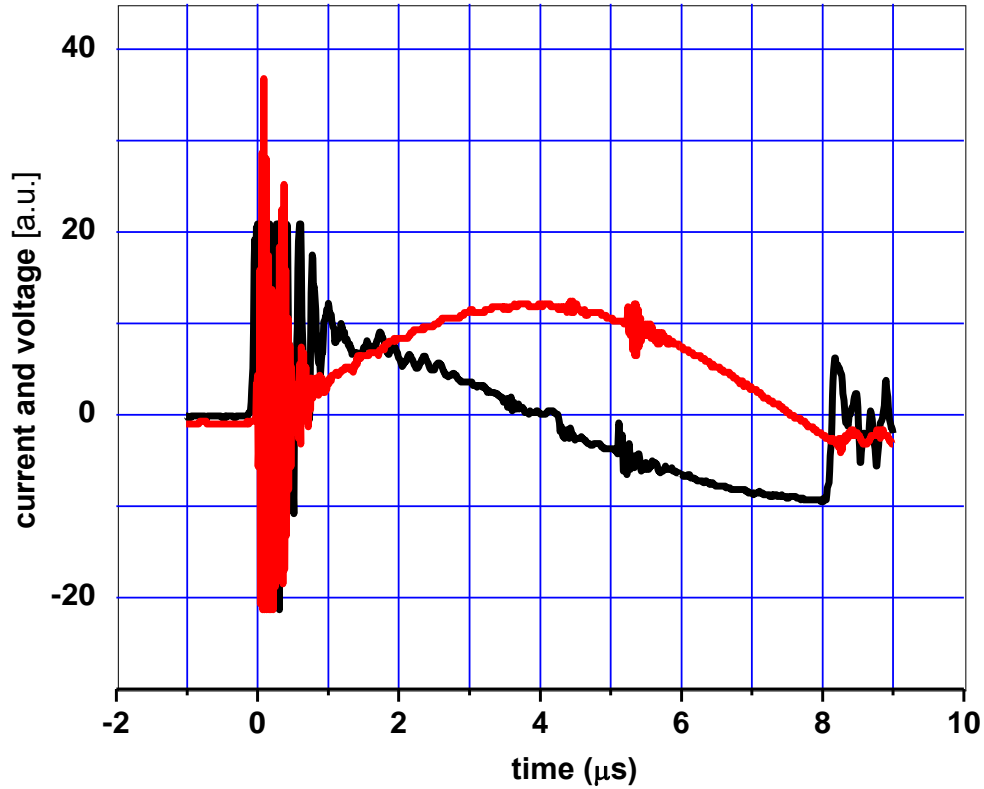


Figure 2. Discharge current (red) and voltage (black) signals from the plasma device.

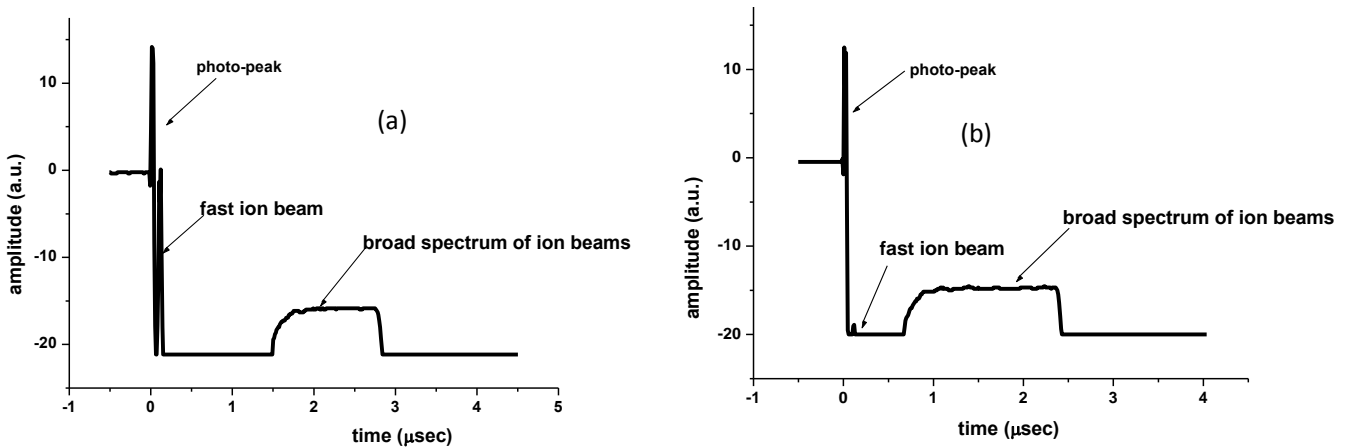


Figure 3. Typical Faraday cup signals obtained from a single discharge left signal (a) indicate good peak of fast ions while right signal shows much smaller fast ions than right one (b).

consequently the best operating pressure for ion detection in this experiment is 0.8 torr. The energy spectrum of helium ion is shown in Figure 5. Data shows two groups of ion spectrum, first group of lower kinetic energy corresponding to helium ion with kinetic energy ranging from 0.3 to 1.0 keV, and second group of higher kinetic value ranging from 15 to 540 keV.

The ion beam of the present image (Figure 6) has a circular cross-sectional area $28 \mu\text{m}^2$. The beam contains a large number of fast ions which are distributed uniformly or quasi-uniformly over the beam cross-section. A majority of quasi-uniform ion density, where the density of ions is distributed in an increasing trend toward the beam center.

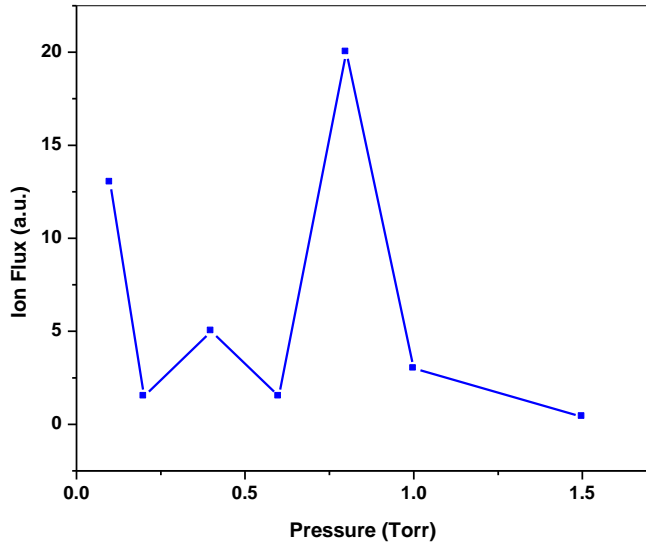


Figure 4. Variation of ion flux with helium gas pressure (torr).

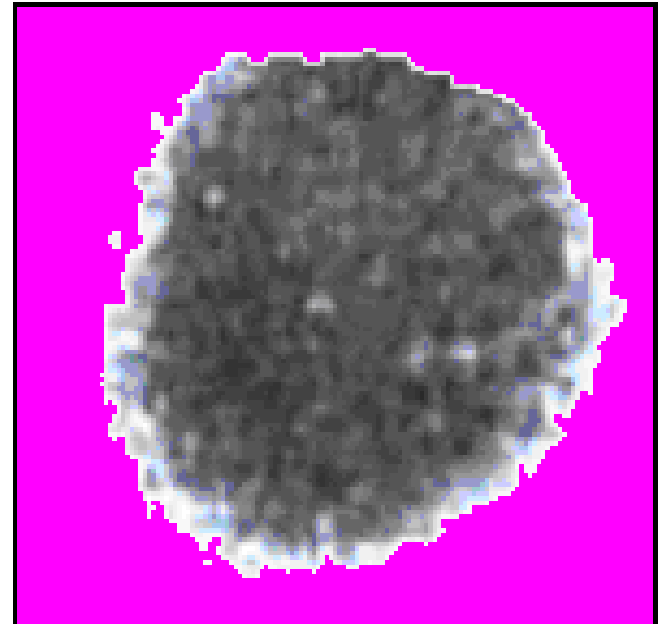


Figure 6. Image of the helium ion tracks (0.8 torr, 15 kV) as obtained from plasma focus discharge with LR-115A film.

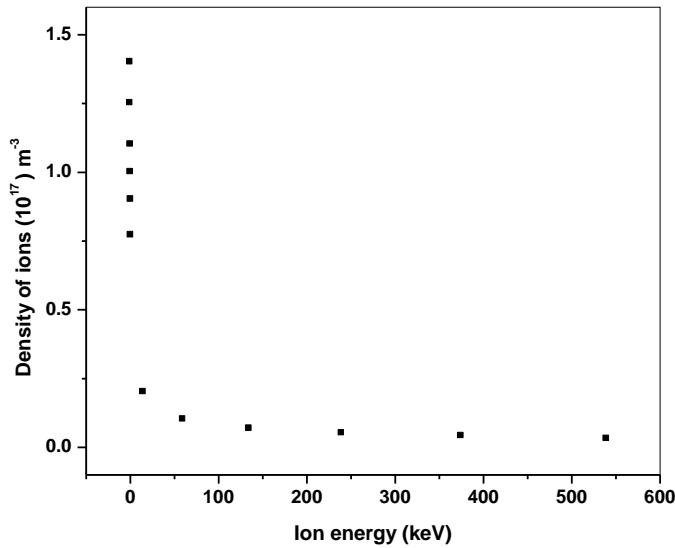


Figure 5. Energy spectrum of ion.

It is possible to estimate the ion flux density of microbeam using a model consisting of a core surrounded by co-central zones (CCZ model) is proposed by EL-Aragi et al. (2007). The registered ion images are obtained for 0.1 J/ 15 kV PF-shots performed at the initial filling gas pressure $P = 0.8$ Torr helium. The total ion emission (centered on Z-axis) is estimated to be 4.47×10^{11} ion/steradian.

The shear in the velocity in conjunction with B_θ will produce centrifugal force which tends to a rotary or vortex pattern. Once the vortex or vortices are setup, the acceleration of plasma is the centrifugal acceleration

which is provided by currents flowing in the direction of rotary motion of the mass of the plasma. The rotational drift velocity is greater for the ions because of their greater mass and hence a net circular current flows will crossed with B_θ to produce a centrifugal acceleration to hold the plasma in the form of an eddy or vortex.

The drift velocity of ions due to viscous forces in rotating plasma provide an azimuthally current density J_θ and an axial magnetic field B_z . The B_z field due to such viscous battery is proportional to the vortices of the fluid. The rotational velocity V_θ is composed of three drifts that is, $E \times B$ drift, diamagnetic drift and centrifugal force drift. The plasma is accelerated not only axially by $J_z \times B_\theta$ force but azimuthally by $J_\theta \times B_z$ force, where J_z is the axial discharge current and B_θ is self-induced azimuthally magnetic field.

Acceleration mechanism

In the radial phase, shock front and the piston starts together at $r=a$ length of the pinch is zero at this time. In any plane the velocity of the shock front is larger than the piston velocity, so the distance between them is a time dependent quantity. The shock front accelerates onto the axis, hitting it; a reflected shock develops and moves in radial outwards (Figure 7). The piston continuous to compress inward until it hits the outgoing reflected shock front. The meeting point between reflected shock and a piston called point of maximum compression of the pinch (minimum radius).

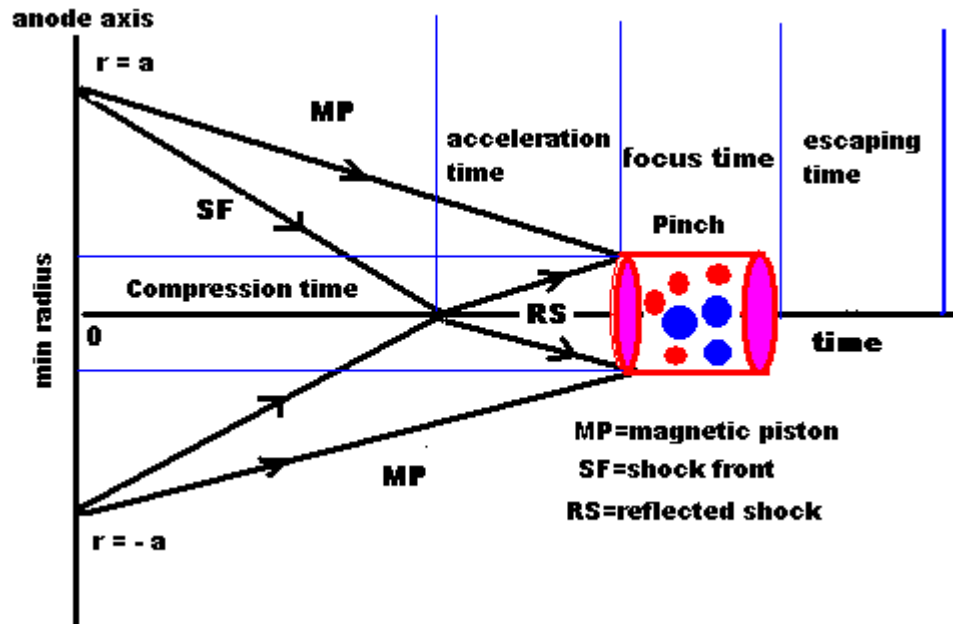


Figure 7. Schematic of radial phase development when magnetic piston separates from.

Compression phase start after transformation of plasma structure to plasma column. This plasma column will compressed adiabatically to form the pinch of final focus. The rapid compression of relatively dense plasma leads to heating plasma to a thermonuclear (fusion) temperature. The plasma collapses toward the center with approximately constant acceleration and flutes which subsequently develop on the outer surface of the plasma are interpreted as Rayleigh-Taylor.

Rayleigh-Taylor instability prevents the compression of the plasma column to get uniformly radial. The magnetic field starts diffusing into the plasma column, leading to an anomalous high plasma resistance as well as increasing the inductance of the system because of increasing the density of plasma column. The sharp change in plasma inductance and high plasma resistance induces high electric field inside the plasma column. This electric field will accelerate the ions and electrons in opposite direction. As result for that, the relative drift between ions and electrons leads to an increasing electron thermal velocity.

If the density clump occurs in plasma, an electric field can cause the ions and electrons to separate, generating another electric field. If there is feedback mechanism that causes the second electric field to enhance the first one, an electric field grows indefinitely and the plasma is unstable. Such instability called drift instability. In some cases, drifts can be self-perpetuating (charge separation leading to a drift, leading to more charge separation and so on), so that plasma instability results.

Generation of high energy particles and radiation in the plasma focus are considered to be an indication of non-

thermodynamic equilibrium of the pinch. The presence of a beam of charged particles that forms in the plasma is explained by the appearance of electric fields which can be caused by the development of a Rayleigh-Taylor instability, plasma turbulence, magneto-acoustic wave propagation in the pinch.

In plasma focus, especially in the pinch phase the plasma gets more compressed at the onset of hydrodynamic instabilities ($m = 0$) as shown in Figure 8 (El-Aragi, 2010). The charged particles (ions and electrons) are trapped between two layers of plasma current sheath which acts like two moving magnetic mirrors with radius R and these particles initially have a velocity V_i (Yousefi et al., 2007), which were observed in the plasma column, a ring-shape around the dense plasma column (necking) that it can be attributed to the ion shape in the pinhole image. In fact, it seems that, $m = 0$ instability (necking) cause the ions acceleration with periods of few to tens of nanoseconds.

During compression phase the plasma density is high, then coulomb collisions between electrons and ions will efficiently thermalise the plasma. The dissipated energy ends up distributed equally amongst the particles, forming a Maxwellian distribution. The particles are accelerated in the current sheath medium as result of many collisions which act as a scattering center. Here the charged particles impinging on the oscillating sheath edge suffer a change of a velocity upon reflection back into the bulk plasma. As the sheath moves into the bulk, the reflected particles gain energy, as the sheath moves away, the particles lose energy. As the particle goes deeper into the sheath which acts as a potential barrier, it

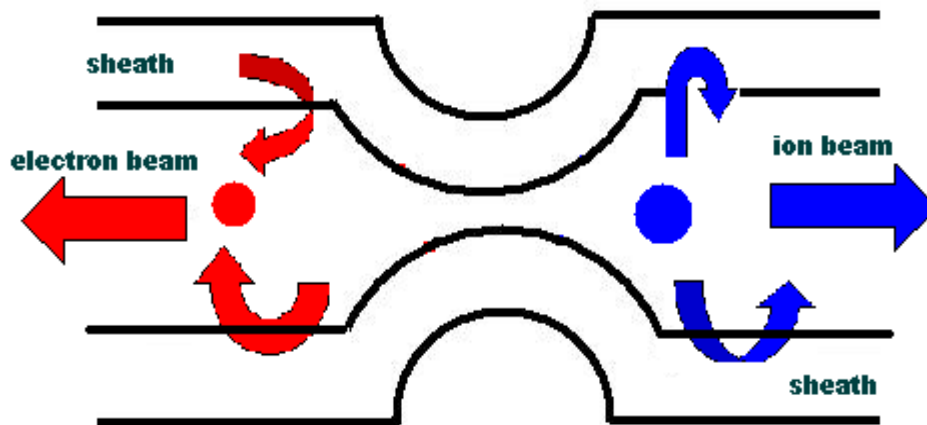


Figure 8. Shows the plasma pinch and emission beams of charged particles onset of instability inducing micro instabilities.

is slowed down by the retarding space charge field. After it has entirely lost its velocity, it turns back and increases its velocity under the action of an accelerating field, returning to the plasma.

Conclusion

Helium ion beam was detected using fast response charge collector system (Faraday cup) and time-integrated solid state nuclear track detector LR-115A. Faraday cup measurements showed that the ion energy spectrum a mixture of faster group of ions that has higher kinetic energy ranging from 15 to 540 keV and slower group that has lower kinetic energy value ranging from 0.3 to 1.0 keV. It is found that the ion flux depend on the filling gas pressure and the maximum ion flux was registered at P = 0.8 Torr of helium gas. The ion flux density has been determined using track etching technique LR-115A. The flux density of ion beam was estimated to be 4.4×10^{11} ion/steradian using CCZ model.

Conflict of Interest

The authors have not declared any conflict of interest.

REFERENCES

Bernstein MJ (1970). Acceleration mechanism for neutron production in plasma focus and Z-pinch discharges. *Phys. Fluids*. 13:2858–2866.
 Deutsch R, Kies W (1988). Ion acceleration and runaway in dynamical pinches. *Plasma Phys. Contr. Fusion*. 30:263–276.
 El-Aragi G (2010). Ion Beam Emission within a Low Energy Focus Plasma (0.1kJ) Operating with hydrogen. *J. Zeitschrift fuer Naturforschung* 65a.(2010).

EL-Aragi GM, Seddik U, Abd EL-Haliem A (2007). Detection of accelerated particles from pulsed plasma discharge using solid state nuclear track detector, *Pramana J. Phys.* 68(4):603-609.
 Gerdin G, Stygar W, Venneri F (1981). Faraday cup analysis of ion beams produced by a dense plasma focus. *J. Appl. Phys.* 52:3269-3275.
 Jager U, Herold H (1987). Fast ion kinetics and fusion reaction mechanism in the plasma focus. *Nucl. Fusion*. 27:407–423.
 Kelly H, Marquez A (1996). Ion-beam and neutron production in a low-energy plasma focus. *Plasma Phys. Contr. Fusion*. 38:1931.
 Lee S, Saw SH (2013). "Plasma focus ion beam fluence and flux-For various gases". *Physics Plasmas*. 20(6).
 Mather JW (1971). Dense plasma focus, *Methods of Experimental Physics Vol 9B*, ed H Lovberg and H R Griem (New York: Academic) pp. 187–249.
 Pasternak A, Sadowski M (1998). Analysis of ion trajectories within a pinch column of a PF-type discharge. In: *Proc ICPP&25th EPS Conf CFPP*. Praha, Czech Republic. ECA 22C:2161–2164.
 Wong CS, Choi P, Leong WS, Singh J (2002). Generation of High Energy Ion Beams from a Plasma Focus Modified for Low Pressure Operation. *Jpn. J. Appl. Phys.* 41:3943-3946.
 Yousefi HR, Nakata Y, Ito H, Masugata K (2007). Characteristic Observation of the ion beams in the plasma focus device. *Plasma Fusion Res.* 2:S1084.
 Zakaullah M, Ijaz A, Murtaza G, Waheed A (1999). Imaging of fusion reaction zone in plasma focus. *Physics of Plasma*. 6:3188.

Full Length Research Paper

Guiding of light with pinholes

Makoto Morinaga

Institute for Laser Science, University of Electro-Communications Chofu, Tokyo, 182-8585 Japan.

Received 30 July, 2014; Accepted 8 October, 2014

A new type of light waveguide using linearly aligned pinholes is presented. Results of basic experiments are compared with theoretical estimates calculated using continuous model. This model predicts that the loss per unit length of the light inside this waveguide is proportional to the square root of the spacing between the pinholes. Since this waveguide utilizes no transparent material, it can be used to guide electromagnetic waves of wide wavelength ranges as well as other waves such as matter waves.

Key words: Waveguide, diffraction optics, atom optics.

INTRODUCTION

Waveguides for electromagnetic fields are widely used to transmit power as well as information. Classical waveguides for electromagnetic fields ranges from coaxial cables for radio frequency (RF) fields, metal waveguides for microwave fields to dielectric waveguides (optical fibers) for optical fields (Cronin, 1995). Among them optical fibers bear extremely low transmission loss and are widely used not only for classical communication (Agrawal, 2010) but also for quantum communication (Gisin, et al., 2006). Also photonic crystals have been implemented recently (Skorobogatiy and Yang, 2009). All of them require special media of high transmissivity and/or high reflectivity. In this paper, we propose a new type of waveguide composed of linearly aligned pinholes of same diameter (Figure 1).

Such a structure is meaningless in geometrical optics since whether a ray transmits through this structure depends only on the geometrical arrangement of the ray and the first and the last pinholes, and pinholes in between play no role for the transmission. However, if we

treat light as wave, it turns out that the transmission loss

at each pinhole has a form $\beta \left(\frac{\lambda L}{a^2} \right)^{\frac{3}{2}}$ where λ is the wavelength of the light, L is the spacing between pinholes, d is the radius of the pinholes, and β is a constant that depends on the order of the transverse mode of the light (Figure 1). Thus the transmission loss per unit length is proportional to \sqrt{L} so that it can in principle be made arbitrarily small by making the spacing L between the pinholes smaller and smaller. Since no special material is required for its construction, it can be used to guide electromagnetic fields of wide frequency ranges, or waves of other kinds such as matter waves. Or it can also be used to guide and/or confine atoms with light guided by this pinhole waveguide because the space where light passes through is vacant. In the following, we present basic experiments with pinhole waveguides and, in the appendix, we will outline a theoretical treatment of this waveguide using continuous model to analyze the

* E-mail: morinaga@ils.uec.ac.jp

Author(s) agree that this article remain permanently open access under the terms of the [Creative Commons Attribution License 4.0 International License](https://creativecommons.org/licenses/by/4.0/)

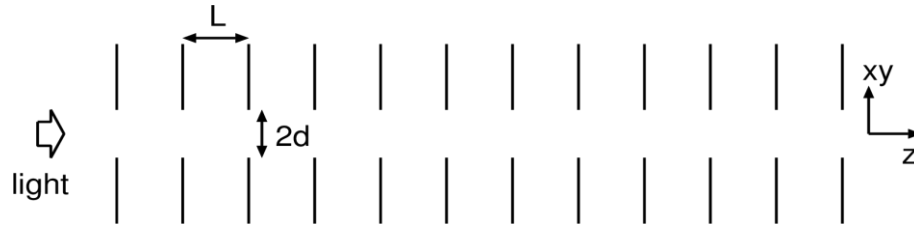


Figure 1. Construction of the pinhole waveguide. Pinholes of radius d are aligned on a straight line with spacing L between the pinholes.

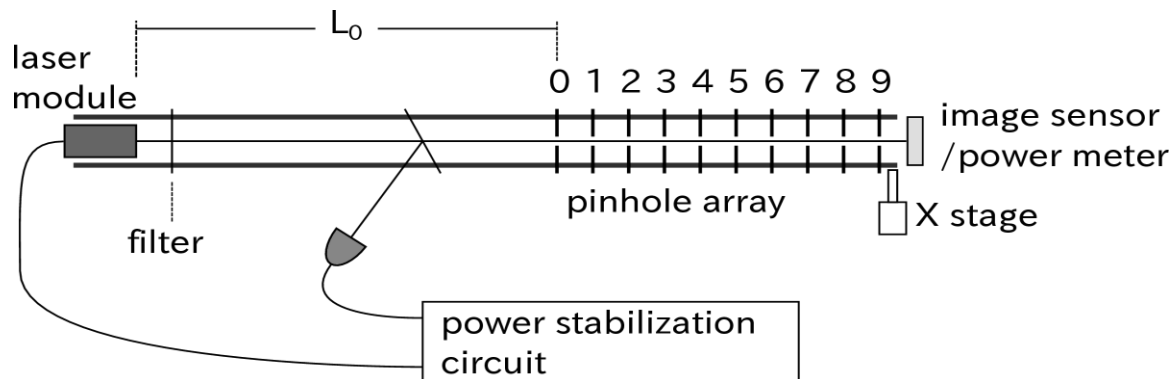


Figure 2. Light from a laser module propagates through pinholes and is detected by either an image sensor or a power meter at the end of the pinhole array which also can be inserted in between the pinholes. Filters are used to select 1064 nm/532 nm wavelengths. The distance L_0 between the laser module and the 1st pinhole is 450 mm.

experimental results. For an array of slits, see (Morinaga, 2014) for asymptotic analysis and numerical simulation that calculate the diffraction directly.

EXPERIMENTS WITH PINHOLE WAVEGUIDES

The experimental setup is schematically shown in Figure 2. A Diode Pumped Solid State (DPSS) laser module generates TEM_{00} output of wavelength at both 1064 and 532 nm. 1064 nm (532 nm) wavelength is selected by inserting a visible cut filter (infrared cut filter). Part of the laser beam is reflected into a photo diode for power stabilization. When the laser beam enters the pinhole array, the beam size is considerably larger than the size of the pinhole and we can regard the incident wave as a spherical wave. Each pinhole is mounted on a xy -translation stage which is fixed on a linear rail lying in z -direction. Up to 10 pinholes can be set on the rail with minimum spacing of 15 mm (29 mm to insert the image sensor or the power meter between the pinholes).

Pinhole alignment

The alignment procedure of the pinholes on a straight line

is as follows. The power meter is always set at the end of the pinhole array during this procedure and the light at 532 nm wavelength is used. First we set no pinhole except the last pinhole (pinhole no.9 in Figure 2) and maximize the power by adjusting the xy -position of this pinhole (the power is plotted as '0' in the horizontal axis of Figure 3). Next we set the first pinhole (pinhole no.0 in Figure 2) and maximize the power by adjusting the xy -position of this pinhole (plotted as '1' in the horizontal axis of Figure 3). And then pinhole no.1 (plotted as '2'), pinhole no.2 (plotted as '3'), and so on. The spacing between the pinholes is $L=45$ mm. The measured values are compared with simulated values obtained by calculating the sequential diffraction by the pinholes. From Figure 3, we see that the transmitted light power increases with increasing number of pinholes, which cannot be explained by geometrical optics.

Propagation through the pinhole array

After setting and aligning all the 10 pinholes light power after each pinhole is measured and compared with the theoretical curve calculated using the Equation (19) in the appendix (Figure 4). In the calculation we neglected the curvature of the wavefront of the input laser so that the

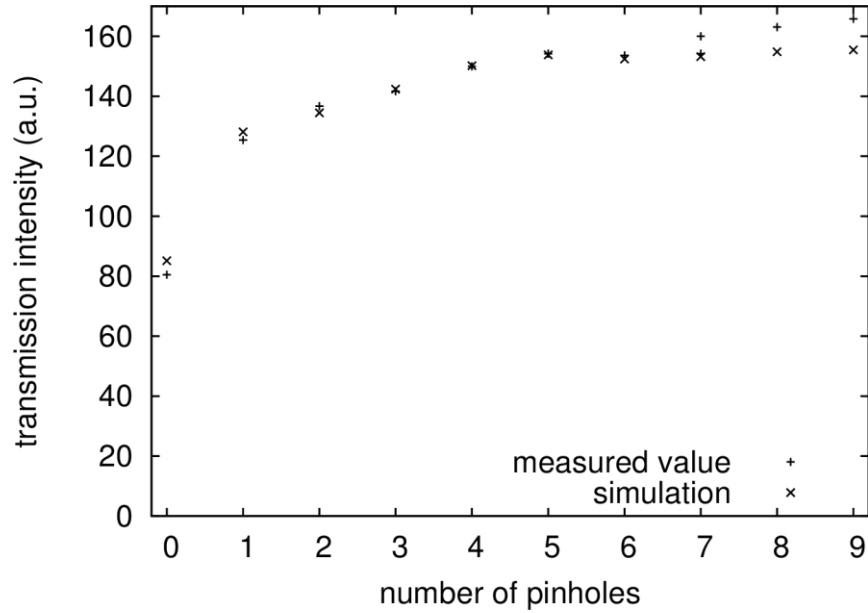


Figure 3. The power of the output of the pinhole array is plotted while inserting pinholes one by one. Pinhole diameter: $2d=0.5$ mm. Light wavelength: $\lambda=532$ nm. Calculated values are also plotted for comparison.

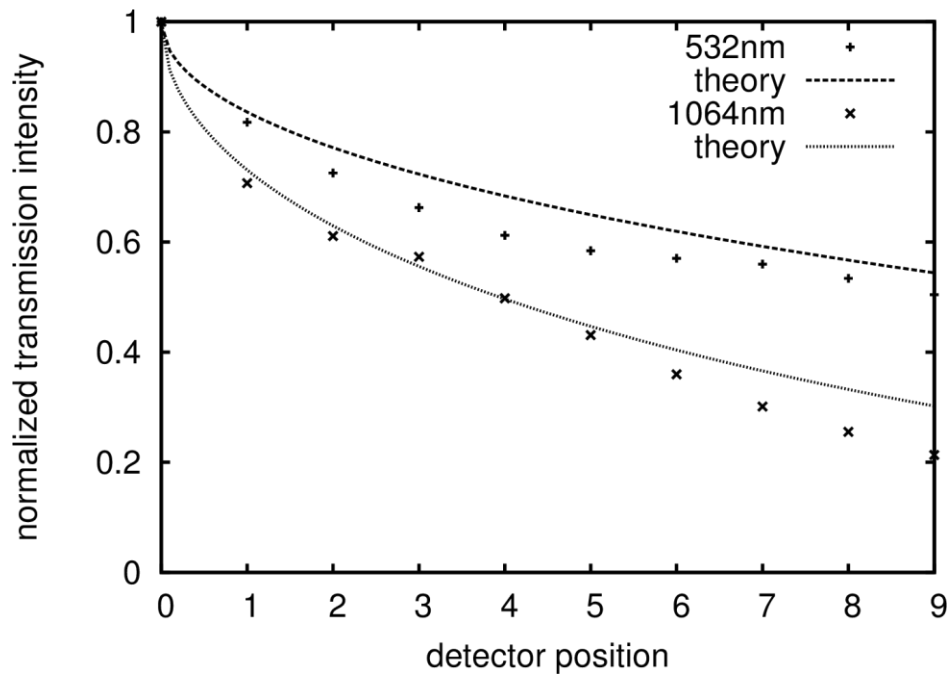


Figure 4. Light power after each pinhole is plotted. The power after the pinhole no.0 is normalized to 1. Pinhole spacing: $L=45$ mm. $2d=0.5$ mm. Two lines are theoretical curves calculated using the continuous model (Equation (19)).

incident wave is assumed to be a plane wave and we used the value of ξ given in Equation (1). The theoretical curves are plotted with no fitting parameter except that the

initial power is normalized to 1 for both experiment and theory. The tendency that the experimental value is lower than the theoretical curve might be explained by the fact

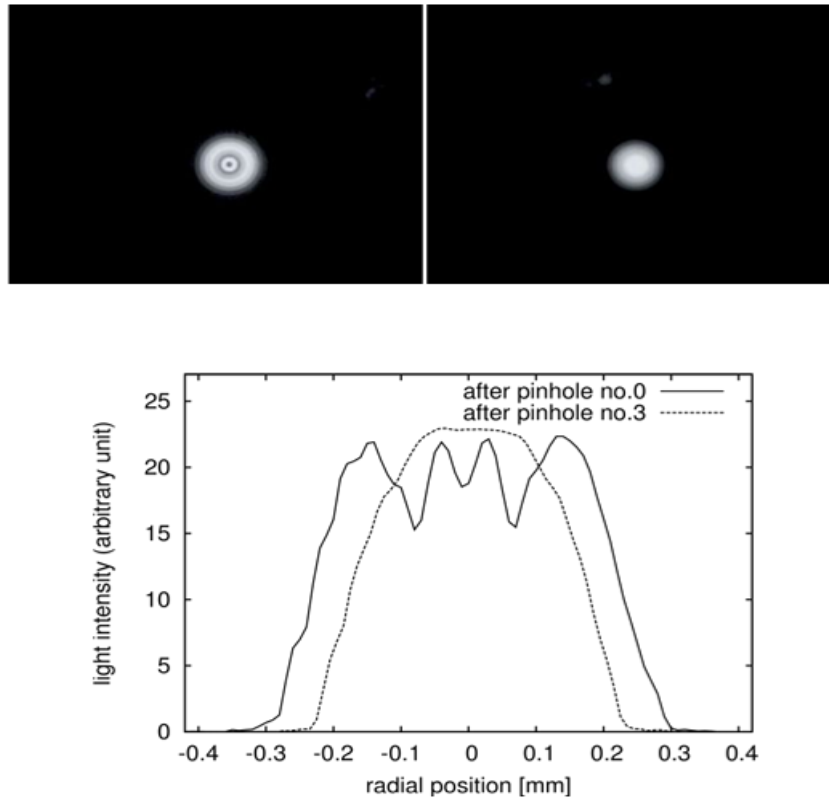


Figure 5. Beam images after pinhole no.0 (left image) and pinhole no.3 (right image). The graph shows their radial distributions.

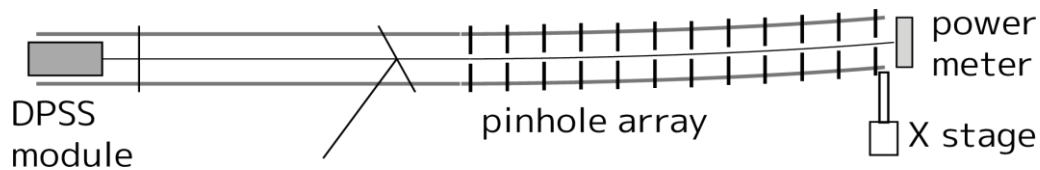


Figure 6. Schematics of the light bending experiment.

that the misalignment of the pinhole always decreases the power from that without misalignment. The initial square beam cut out from the incident plane wave contains high order transverse modes that attenuate fast compared with the lower order mode leading to the initial rapid decay. After propagating through several pinholes, lowest order mode dominates, then showing slower decay.

In Figure 5 beam images after the pinhole no.0 and no.3 are shown ($\lambda=532$ nm). The latter shows smooth profile with a peak intensity at the center which qualitatively confirms the explanation given above (the distance of about 17 mm from the pinhole to the image sensor makes fine structure in the left image due to diffraction).

Bending of light

The linear rail on which pinholes is sitting is fixed to the

optical table at three points: at the left end, in the middle near the pinhole no.0, and at the right end. We remove the fixing screw at the right end and push this end to the transverse direction so that the rail is bent elastically (Figure 6).

In Figure 7 we plot the power of the output light versus the displacement of the last pinhole (pinhole no.9). The experimental value is compared with a theoretical curve assuming the geometrical optics.

Certain amount of light is transmitted even with displacements larger than the diameter of the pinhole (0.5 mm). The measured values are also compared with a theoretical curve using a simplified model: the guided light experiences several (additional) reflections inside the waveguide when the waveguide is bent. Sum of the reflection angle Θ_j (measured from the reflection surface) is equal to a half of the bending angle Θ of the

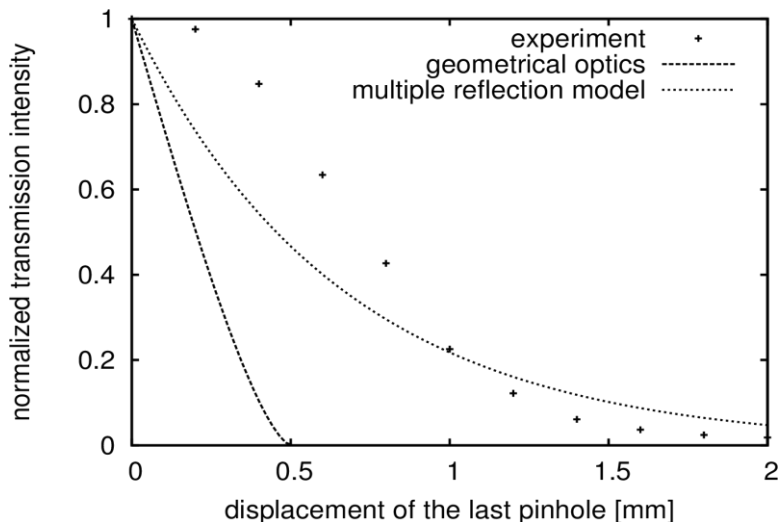


Figure 7. Power of the transmitted light is measured while bending the waveguide. $2d=0.5$ mm. $\lambda=532$ nm. $L=45$ mm. Dotted line is the theoretical curve following the geometrical optics. The measured values are also compared with a theoretical curve.

waveguide at the output end: $\sum_i \Theta_i = \Theta/2$. The power loss at each reflection is known to be $4\sqrt{\pi L/\lambda}\Theta_i$ when $\Theta_i \ll \sqrt{\lambda L}$ (Kouznetsov and Oberst, 2005b). The final output power I is calculated as $I = I_0 \prod_i \exp(-4\sqrt{\pi L/\lambda}\Theta_i) = I_0 \exp(-2\sqrt{\pi L/\lambda}\Theta) = I_0 \exp(-\sqrt{\pi L/\lambda} \frac{3\delta}{L_1})$ where I_0 is the input power, δ is the transverse displacement at the output end, and $L_1=405$ mm is the total length of the waveguide. Here we also used the relation $\Theta = \frac{3\delta}{2L_1}$ derived from the elementary mechanics.

The agreement is acceptable taking into account that no fitting parameter is used in the calculation although the discrepancy is apparent when the displacement is small. This is because the model does not include the notion of mode spacing which would prevent mixing of modes for small bending.

CONCLUSION AND OUTLOOK

In this paper we presented basic experiments of light guiding with a pinhole array. A theoretical study using a continuous model was also developed which predicts that the loss per unit length is proportional to the square root of the spacing between the pinholes. The experimental results roughly confirm the theoretical estimates. However, further study is needed to understand the details of this new waveguide, such as how the thickness of the

pinholes affects the transmission. Also a refined theory is needed to explain the transmission behavior quantitatively when the pinhole array is bent.

Conflict of Interest

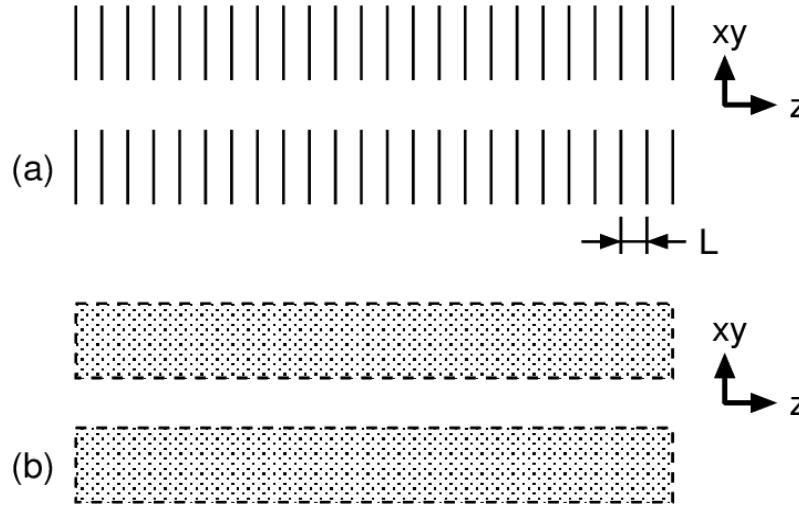
The authors have not declared any conflict of interest.

ACKNOWLEDGEMENT

This work was partly supported by the AMADA FOUNDATION and the Photon Frontier Network Program (MEXT).

REFERENCES

- Agrawal GP (2010). Fiber-Optic Communication Systems, 4th ed., John Wiley & Sons.
- Cronin N J (1995). Microwave and Optical Waveguides, CRC Press.
- Gisin N, Iblisdir S, Tittel W, Zbinden H (2006). Quantum Communications with Optical Fibers, in: A. V. Sergienko (Eds.), Quantum Communications and Cryptography, Taylor & Francis Chapter 2.
- Kouznetsov D, Morinaga M (2012). Guiding of waves between absorbing walls. J. Mod. Phys. 3 553. <http://dx.doi.org/10.4236/jmp.2012.37076>
- Kouznetsov D, Oberst H (2005a). 1. Reflection of waves from a ridged surface and the Zeno effect, Opt. Rev. 12: 363. <http://dx.doi.org/10.1007/s10043-005-0363-9>
- Kouznetsov D, Oberst H (2005b). 2. D. Kouznetsov and H. Oberst, Scattering of waves at ridged mirrors, Phys. Rev. A 72: 013617. <http://dx.doi.org/10.1103/PhysRevA.72.013617>
- Morinaga M (2014). Wave propagation through an array of slits, arXiv:1409.6865
- NIST Digital Library of Mathematical Functions §10.17. <http://dlmf.nist.gov/10.17>
- Skorobogatiy M, Yang J (2009). Fundamentals of Photonic Crystal Guiding, Cambridge University Press.



Appendix Figure 1. (a) Array of masks separated by L . (b) The mask array is replaced with continuous absorbing medium.

APPENDIX

Continuous model

Dealing directly with a discrete array of masks (pinholes, slits,...) for theoretical analysis is not an easy task. Instead, we introduce in this appendix a model in which the discrete set of masks is replaced with continuous medium of some absorbance that fills the closed region of the masks (Appendix Figure 1). This continuous model was first introduced for an array of half-planes to account the enhanced quantum reflection of matter waves from the ridged surfaces (Kouznetsov and Oberst, 2005a). The lowest order transverse mode function for the slit array and its loss parameter are also calculated already (Kouznetsov and Morinaga, 2012). Here we will determine all the transverse mode functions and their propagation parameter for the case of the slit array and the pinhole array. The light field is treated as a scalar field (scalar theory). The wave equation for this model is given by

$$-k_0^2 \psi(x, y, z) = \{1 - i\epsilon \Theta(x, y)\} \nabla^2 \psi(x, y, z)$$

where k_0 is the wavenumber of light, $\Theta(x, y)$ is a step function that takes value 1 (0) in the closed (open) region of masks, and ϵ is a positive constant related to the absorbance of the medium. As we shall see below $\epsilon \ll 1$ for our system under consideration. First we consider a plane wave propagating through the area filled uniformly with such absorbing medium. Taking z -axis as the direction of propagation, the wave equation is written as:

$$-k_0^2 \psi(z) = (1 - i\epsilon) \psi''(z).$$

Its solution is given by

$$\psi(z) = e^{ik_z z}$$

with $k_0^2 = (1 - i\epsilon) k_z^2 \approx \left\{ \left(1 + \frac{i}{2\epsilon}\right)^{-1} k_z \right\}^2$ so that $k_z = \left(1 + \frac{i}{2\epsilon}\right) k_0$ and $|\psi(z)|^2 = e^{-\zeta_0 z}$ with the intensity absorbance $\zeta_0 = \epsilon k_0$. Given that this absorbing medium imitates a stack of opaque masks separated by a distance L , we expect that $\zeta_0 \sim \frac{1}{L}$ so that $\epsilon \sim \frac{1}{k_0 L}$. Thus we shall

write $\epsilon = \frac{\xi}{k_0 L}$ with a positive parameter ξ of order of 1.

We consider the parameter region where the separation of masks L is much larger than the wavelength, so that $\epsilon \ll 1$. The continuous model itself cannot determine the value of ξ (or ϵ). By comparing the attenuation of a wave propagating in a slit waveguide calculated using continuous model with that calculated with direct method (Morinaga, 2014) it is shown that

$$\xi = \frac{9}{2\pi}. \quad (1)$$

A.1 Slit array

Consider an array of slits of opening width $2d$ (open for $|x| < d$). The wave equation is written as:

$$-k_0^2 \psi(x, z) = \{1 - i\epsilon \Theta(x^2 - d^2)\} (\partial_x^2 + \partial_z^2) \psi(x, z)$$

where Θ is the conventional step function defined as:

$$\Theta(s) \equiv \begin{cases} 0 (s < 0) \\ 1 (s \geq 0) \end{cases}$$

Because of the translational symmetry in z-axis direction, we can assume the form of the solution as $\psi(x,z) = \phi(x) e^{ik_z z}$ (a general solution is the sum of such solutions). Below we also assume that the wave propagates nearly in z direction so that $k_z \approx k_0$.

Region A (inside the opening of slits) $|x| \leq d$

The wave equation for the transverse wavefunction $\phi(x)$ here is

$$-(k_0^2 - k_z^2)\phi(x) = \phi''(x)$$

with a solution

$$\phi(x) = cs(k_A x),$$

where cs is defined as

$$cs(u) = \begin{cases} \cos u & (\text{even parity mode}) \\ \sin u & (\text{odd parity mode}) \end{cases} \quad (2)$$

and k_A satisfies $k_0^2 = k_A^2 + k_z^2$. We are considering the situation in which the wave is nearly confined in the opening region $|x| \leq d$ and hence $\phi(\pm d) \approx 0$, so that

$$k_A d \approx \frac{n+1}{2} \pi \quad (n=0, 1, 2, \dots)$$

provided that we use \cos (\sin) in (2) for even (odd) n . Defining $k_n \equiv \frac{n+1}{2d} \pi$ and write $k_A = k_n + \beta + i\gamma$ with real numbers β and γ , then $|\beta d| \ll 1$ and $|\gamma d| \ll 1$.

$$\phi(\pm d) = cs(\pm k_A d) \approx \pm (\beta + i\gamma) d cs'(\pm k_n d)$$

$$\phi'(\pm d) = k_A cs'(\pm k_A d) \approx k_n cs'(\pm k_n d)$$

$$\left. \frac{\phi'}{\phi} \right|_{x=\pm d} \approx \pm \frac{k_n}{(\beta + i\gamma)d} \quad (3)$$

Region B (outside the opening of slits): $|x| \geq d$

Here the wave equation is

$$-\{k_0^2 - (1-i\epsilon)k_z^2\}\phi(x) = (1-i\epsilon)\phi''(x)$$

so that the solution is, taking into account that it should not diverge when $x \rightarrow \pm\infty$,

$$\phi(x) \propto e^{ik_B |x|} \quad (4)$$

where k_B satisfies $k_0^2 = (1-i\epsilon)(k_B^2 + k_z^2)$ and $\text{Im } k_B > 0$ (the proportionality factor in Equation (4) has opposite sign for $x \geq d$ and $x \leq -d$ for the odd parity solution). Thus

$$\left. \frac{\phi'}{\phi} \right|_{x=\pm d} = \pm ik_B \quad (5)$$

Boundary condition at $x = \pm d$

By requiring $\phi(x)$ and $\phi'(x)$ is continuous at $x = \pm d$, from Equations (3) and (5) we find

$$ik_B = \frac{k_n}{(\beta + i\gamma)d} \quad (6)$$

By noting $k_B^2 - k_A^2 = \frac{i\epsilon}{1-i\epsilon} k_0^2$ and $|k_B| = \frac{|k_n|}{|\beta + i\gamma|d} \gg |k_n| \approx |k_A|$, we see

$$k_B^2 \approx i\epsilon k_0^2 \quad (7)$$

so that

$$k_B = \frac{1+i}{\sqrt{2}} \sqrt{\epsilon} k_0 \quad (8)$$

Using Equation (6)

$$\beta + i\gamma = \frac{k_n}{ik_B d} = \frac{1+i}{\sqrt{2}} \frac{k_n}{\sqrt{\epsilon} k_0 d}$$

and we obtain

$$k_A = k_n + \beta + i\gamma = \left(1 - \frac{1+i}{\sqrt{2\epsilon} k_0 d}\right) k_n \quad (9)$$

From the assumption that $|\beta d| \ll 1$ and $|\gamma d| \ll 1$ we see $\sqrt{\epsilon} k_0 d \gg 1$, that is,

$$\frac{L}{k_0 d^2} = \frac{1}{2\pi} \frac{\lambda L}{d^2} \ll 1 \quad (10)$$

Finally k_z is derived as

$$k_z = \sqrt{k_0^2 - k_A^2} \approx k_0 - \frac{1}{2} \frac{k_A^2}{k_0} \approx k_0 - \frac{k_n^2}{2k_0} + \frac{k_n^2}{\sqrt{2\varepsilon} k_0^2 d} \quad (11)$$

From this we calculate the light attenuation along the waveguide

$$|e^{ik_z z}|^2 = e^{-\zeta z}$$

where the attenuation coefficient $\zeta = 2\text{Im} k_z$ is calculated as

$$\zeta = \frac{\sqrt{2} k_n^2}{\sqrt{\varepsilon} k_0^2 d} = (n+1)^2 \frac{\sqrt{2} \pi^2}{4 \sqrt{\varepsilon} k_0^2 d^3} = (n+1)^2 \frac{\sqrt{2L} \pi^2}{4 \sqrt{\varepsilon} k_0^3 d^3}$$

using $\varepsilon = \frac{\xi}{k_0 L}$. The attenuation per length L (that is, per one slit) ζL can be written as a function of a single dimensionless parameter $\frac{\lambda L}{d^2}$:

$$\zeta L = (n+1)^2 \frac{\sqrt{2} \pi^2}{4 \sqrt{\xi}} \left(\frac{L}{k_0 d^2} \right)^{\frac{3}{2}} = (n+1)^2 \frac{\sqrt{\pi}}{8 \sqrt{\xi}} \left(\frac{\lambda L}{d^2} \right)^{\frac{3}{2}} \quad (12)$$

A.2 Pinhole array

In the case of an array of pinholes of diameter d , using cylindrical coordinate (r, φ, z) , the wave equation is written as

$$-k_0^2 \psi(r, \varphi, z) = \{1 - i\varepsilon \Theta(r^2 - d^2)\} \left(\partial_r^2 + \frac{1}{r} \partial_r + \frac{1}{r^2} \partial_\varphi^2 + \partial_z^2 \right) \psi(r, \varphi, z).$$

In the same way as in the case of slit array, we shall derive a solution of the form $\Psi(r, \varphi, z) = \phi(r, \varphi) e^{ik_z z}$ with $k_z \approx k_0$.

Region A (inside the opening of pinholes): $|r| \leq d$

The wave equation

$$-(k_0^2 - k_z^2) \phi(r, \varphi) = \left(\partial_r^2 + \frac{1}{r} \partial_r + \frac{1}{r^2} \partial_\varphi^2 \right) \phi(r, \varphi)$$

is solved using the Bessel functions of the 1st kind J_m ($m=0, \pm 1, \pm 2, \dots$):

$$\phi(r, \varphi) = J_m(k_A r) e^{im\varphi}$$

where k_A satisfies $k_0^2 = k_A^2 + k_z^2$. Again we postulate

$k_A d \approx \varrho_n^{(m)}$ ($n=0, 1, 2, \dots$). Here $\varrho_0^{(m)}, \varrho_1^{(m)}, \varrho_2^{(m)}, \dots$ are positive zeros of $J_m(\varrho)$ sorted in

ascending order. We define $k_n^{(m)} \equiv \frac{\varrho_n^{(m)}}{d}$ and write

$k_A = k_n^{(m)} + \beta + i\gamma$ using real numbers β and γ with $|\beta d| \ll 1$ and $|\gamma d| \ll 1$.

$$\phi(d, \varphi) = J_m(k_A d) e^{im\varphi} \approx (\beta + i\gamma) d J_m'(k_n d) e^{im\varphi}$$

$$\partial_r \phi|_{(d, \varphi)} = k_A J_m'(k_A d) e^{im\varphi} \approx k_n^{(m)} J_m'(k_n^{(m)} d) e^{im\varphi}$$

$$\left. \frac{\partial_r \phi}{\phi} \right|_{(d, \varphi)} \approx \frac{k_n^{(m)}}{(\beta + i\gamma) d} \quad (13)$$

Region B (outside the opening of pinholes): $|r| \geq d$

The wave equation is written as:

$$-\{k_0^2 - (1 - i\varepsilon) k_z^2\} \phi(r, \varphi) = (1 - i\varepsilon) \left(\partial_r^2 + \frac{1}{r} \partial_r + \frac{1}{r^2} \partial_\varphi^2 \right) \phi(r, \varphi)$$

so that the solution is given by

$$\phi \propto H_m^{(1)}(k_B r) e^{im\varphi}$$

if we take into account its behavior when $r \rightarrow \infty$ ($H_m^{(1)}$ are the Hankel functions of the 1st kind). Here k_B satisfies $k_0^2 = (1 - i\varepsilon)(k_B^2 + k_z^2)$. Noting that $k_B^2 d^2 - k_A^2 d^2 = \frac{i\varepsilon}{1 - i\varepsilon} k_0^2 d^2$ and that the absolute value of the right-hand side is much larger than 1 (Equation (10)) whereas $k_A d$ in the left-hand side is of order of 1 so that we can neglect this term and Equations (7) and (8) holds as in the case of slit array.

From these we see that $|k_B d| \gg 1$ and $\arg(k_B d) \approx \frac{\pi}{4}$ (and thus $-\pi < \arg(k_B d) < 2\pi$), so that we can use the following

asymptotic form of $H_n^{(1)}$ for $\varrho = k_B d$ (see (NIST)):

$$H_m^{(1)}(\varrho) \approx \sqrt{\frac{2}{\pi \varrho}} \exp\left(i \left[\varrho - \frac{2m+1}{4} \pi \right]\right)$$

$$H_m^{(1)'}(\varrho) \approx i \sqrt{\frac{2}{\pi \varrho}} \exp\left(i \left[\varrho - \frac{2m+1}{4} \pi \right]\right)$$

Which lead to

$$\left. \frac{\partial_r \phi}{\phi} \right|_{(d, \varphi)} = ik_B \quad (14)$$

Boundary condition at $r=d$

Continuity of $\phi(r, \varphi)$ and $\partial_r \phi(r, \varphi)$ at $r=d$ yields, from Equations (13) and (14),

$$ik_B = \frac{k_n^{(m)}}{(\beta + i\gamma)d} \quad (15)$$

Equation (15) has the same form as Equation (5) with k_n replaced by $k_n^{(m)}$, so that similar to the case of slit array, we obtain

$$k_A = k_n^{(m)} + \beta + i\gamma = \left(1 - \frac{1+i}{\sqrt{2\epsilon}k_0 d}\right) k_n^{(m)}$$

$$k_z = \sqrt{k_0^2 - k_A^2} \approx k_0 - \frac{k_n^{(m)2}}{2k_0} + \frac{k_n^{(m)2}}{\sqrt{2\epsilon}k_0 d} i$$

From this the attenuation of light along the waveguide

$$|e^{ik_z z}|^2 = e^{-\zeta z}$$

is calculated giving the attenuation coefficient $\zeta = 2\text{Im} k_z$ as

$$\zeta = \frac{\sqrt{2}k_n^{(m)2}}{\sqrt{\epsilon}k_0^2 d} = \frac{\sqrt{2}\varrho_n^{(m)2}}{\sqrt{\epsilon}k_0^2 d^3} = \frac{\sqrt{2}L\varrho_n^{(m)2}}{\sqrt{\epsilon}k_0^3 d^3} \quad (16)$$

and the attenuation per length L (that is, per one pinhole) ζL is given by

$$\zeta L = \frac{\sqrt{2}\varrho_n^{(m)2}}{\sqrt{\epsilon}} \left(\frac{L}{k_0 d^2}\right)^{\frac{3}{2}} = \frac{\varrho_n^{(m)2}}{2\sqrt{\epsilon}\pi^3} \left(\frac{\lambda L}{d^2}\right)^{\frac{3}{2}} \quad (17)$$

Note that the modes with the same transverse wavenumber k_{\perp} ($k_{\perp} = k_n = \frac{n+1}{2d}\pi$ in Equation (12) for

the slits and $k_{\perp} = k_n^{(m)} = \frac{\varrho_n^{(m)2}}{d}$ in Equation (17) for the pinholes) have the same decay parameter.

A.3 Attenuation of a multi-transverse-mode light

In the previous section we estimated the attenuation of a single transverse mode wave. Each transverse mode is specified by a pair (m, n) of an integer m and a non-negative integer n , and if the wave is confined tightly enough in the pinhole waveguide, the transverse mode functions are given by

$$\phi_{mn}(r, \varphi) = \begin{cases} \alpha_{mn} J_m(k_n^{(m)} r) e^{im\varphi} & (r \leq d) \\ 0 & (r > d) \end{cases}$$

(α_{mn} are the normalization factors). Note that these are the Bessel beam transverse mode functions clipped at one of their nodes in the radial direction. The orthonormal condition is written as

$$\delta_{mm'} \delta_{nn'} = \langle \phi_{mn}, \phi_{m'n'} \rangle = \int_0^{\infty} r dr \int_0^{2\pi} d\varphi \phi_{mn}^*(r, \varphi) \phi_{m'n'}(r, \varphi).$$

Here, we consider, as an example, the case where a plane wave $\psi_p = \frac{1}{\sqrt{\pi d^2}} e^{ik_0 z}$ is incident into the

waveguide, and calculate how the wave attenuates while it propagates along the waveguide. The incident wavefront is cut out at the input end of the waveguide (we take the input end as $z=0$) giving the transverse wave function as

$$\phi_p(r, \varphi) = \frac{1}{\sqrt{\pi d^2}} \Theta(d^2 - r^2)$$

and such wavefront is, from the symmetry consideration, expanded with only $m=0$ modes:

$$\phi_p = \sum_{n=0}^{\infty} \beta_n \phi_{0n} \quad (18)$$

By integrating the square of absolute value of both sides of the above equation in (r, φ) plane, we see that

$$\sum_{n=0}^{\infty} |\beta_n|^2 = 1. \text{ The power attenuation is given by}$$

$$P(z) = \sum_{n=0}^{\infty} |\beta_n|^2 \exp(-\zeta_n^{(0)} z). \quad (19)$$

Here $\zeta_n^{(m)}$ is ζ given in Equation (16). By taking inner product of both sides of Equation (18) with ϕ_{0n} ,

$$\beta_n = \langle \varphi_{0n}, \varphi_p \rangle = 2\pi\alpha_{0n}^* \frac{1}{\sqrt{\pi d^2}} \int_0^d r dr J_0(k_n^{(0)} r) = \frac{2\sqrt{\pi}\alpha_{0n}^*}{k_n^{(0)}} J_1(\varrho_n^{(0)}) = \frac{2}{\varrho_n^{(0)}}$$

Here we used $\frac{d}{d\varrho}(\varrho J_1(\varrho)) = \varrho J_0(\varrho)$ and the value of α_{0n} derived in the next subsection (20).

A.4 Normalization factors α_{0n}

From the normalization conditions of ϕ_{0n} we find

$$1 = \langle \phi_{0n}, \phi_{0n} \rangle = 2\pi|\alpha_{0n}|^2 \int_0^d r dr J_0^2(k_n^{(0)} r) = \pi|\alpha_{0n}|^2 d^2 J_1^2(\varrho_n^{(0)}).$$

Here we used the formula

$$\frac{d}{d\varrho} \left\{ \varrho^2 \frac{J_0(\varrho)^2 + J_1(\varrho)^2}{2} \right\} = 2\varrho J_0(\varrho)^2$$

and $J_0(\varrho_n^{(0)}) = 0$. α_{0n} are determined as, besides the phase factor,

$$\alpha_{0n} = \frac{1}{\sqrt{\pi d} J_1(\varrho_n^{(0)})}. \quad (20)$$

Full Length Research Paper

Chemical composition and antioxidant capacity of the leaf extract of *Justicia insularis*

O. T. Adeyemi and O. Babatunde*

¹Department of Chemical Sciences, Ajayi Crowther University, Oyo, Oyo state, Nigeria.

Received 3 December, 2012; Accepted 20 October, 2014

The leaves of *Justicia insularis* have been generating a lot of interest among the Yoruba people in the Southern Nigeria. They provide useful source of human nutrition and medicinal value. In this study, *J. insularis* leaves were harvested, processed and analysed to determine their chemical compositions and also to investigate their antioxidant properties. The proximate analysis showed that the sample contained 15.955% ash, 4.48% crude protein, 2.144% lipid and 18.367MJ/kg energy. The contents of calcium, potassium, phosphorous and magnesium were 3.30, 1.68, 0.11, and 0.76, respectively, while the amounts of sodium, manganese, iron, copper and zinc were 631.04, 334.02, 4490.08, 6.31 and 49.72 mg/g, respectively. The free radical scavenging activity of ethanol extract of *J. insularis* was determined by three methods namely: scavenging effect on 2,2-diphenyl-1-picrylhydrazyl radical (DPPH), hydroxyl radical and peroxide oxidation. Comparison of the results obtained with the three antioxidant standards used in the assay revealed that the ethanol extract of the plant possessed antioxidant activity. The results obtained revealed high value of iron in the leaf and free radical scavenging properties indicating the presence of primary antioxidants in the plant.

Key words: Antioxidants, chemical composition, free radical, *Justicia insularis*.

INTRODUCTION

Most tropical African countries are blessed with diversity of food stuffs which play a basic role in nutrition and healthy body development. Unfortunately, millions of people in developing countries still suffer from malnutrition especially infants and children of rural areas (WHF, 2005). Malnutrition can be tremendously reduced by consuming the foods that are rich in energy, proteins, iron and vitamins, most especially those from the rural environment (Richard et al., 2007). In order to have a healthy population the relation between food, nutrition and health should be reinforced (Atasi et al., 2009). One way of achieving this is through the exploitation of

available local resources such as local indigenous vegetable, since human population in Africa largely depend on edible indigenous vegetables to supplement their minerals and vitamins (Achu et al., 2005).

Numerous vegetables, crops, spices and medicinal herbs have been studied in an effort to identify new and potentially useful antioxidants (Vinson et al., 1998; Ganthavorn and Hughes, 1997; Jitoe et al., 1992; Zheng and Wang 2001). More recently, it has become evident that phenolic natural products may reduce oxidative stress by indirect antioxidant action. For example, various flavonoids, which are found naturally in fruits, vegetables

*Corresponding author. E-mail: toyeenbab@yahoo.com, Tel: +234803455911.

Author(s) agree that this article remain permanently open access under the terms of the [Creative Commons Attribution License 4.0 International License](http://creativecommons.org/licenses/by/4.0/)

and some beverages, have been demonstrated to exert antioxidant effects through a number of different mechanisms (Nijveldt et al., 2001). Knowledge of nutritional and medicinal status of local soup ingredients and food stuffs is important in order to encourage their cultivation and consumption. *Justicia insularis* is an annual or perennial herb up to 2 m tall. Stems are angular, basal part often swollen with aerial root. Leaves are decussately opposite. This herbaceous plant occurs in a wide range of habitats from moist forest to dry savannah regions (Enoch et al., 2009). It is used to make vegetable soup or eaten cooked as spinach. In Western Cameroon, it is added to groundnut soup, while extracts of the boiled leaves are given to babies to loosen their bowels and the leaves are applied to wounds to promote healing in Togoland and North East Ghana (Hepper, 1965).

The neglect of some local vegetables coupled with the growing reduction in their consumption prompted this research.

Therefore, the aim of this work is to assess the chemical composition and antioxidant properties of *J. insularis* in order to ascertain its nutritional suitability as well as health benefits.

MATERIALS AND METHODS

Sampling and sample preparation

Fresh samples of *J. insularis* were collected from different locations at Federal College of Education (Special), Oyo and referenced at the Forest Research Institute of Nigeria Ibadan, Oyo State. The samples were washed with clean water and air-dried for 2 weeks. The dried samples were ground into fine powder with electric grinder and stored in a well labelled air tight polythene bag for further analysis.

Proximate analysis

Crude fat was extracted by the Soxhlet method with petroleum ether (40 to 60°C) for 8 h. Crude nitrogen was determined based on the Kjeldhal procedure and crude protein value was obtained by multiplying the nitrogen value by a factor of 6.25. These, as well as energy and total ash content were estimated as described by the Association of Official Analytical Chemistry (AOAC, 1990).

Mineral analysis

The sample was digested into solution by wet digestion using a mixture of conc. Nitric, perchloric and sulphuric acids in the ratio 9:2:1, respectively. Fe, Zn, Cr, Co, Mg, Ca, Cu, Mn and Pb were determined by Atomic absorption spectroscopy (AAS), Na and K were determined using Atomic Emission Spectrometer and colorimetric method was used to determine phosphorus.

Antioxidant activities

Free radical scavenging assay

The free radical scavenging activity of ethanol extract of *J. insularis*

was measured by 2,2-diphenyl-1-picrylhydrazyl radical (DPPH) according to Blois method (Blois, 1958). An aliquot of DPPH (1 ml, 0.1 mM) solution in methanol was added to 3 ml of ethanol extract of *J. insularis* (100 µg/ml) in water, shaken vigorously, allowed to stand for 10 min in the dark and the absorbance was measured at 517 nm in an ultraviolet (UV)-visible spectrophotometer. Gallic acid was used as positive control. The percentage DPPH scavenging effect was calculated as follows:

$$(\%) A_{\text{cont}} - A_{\text{test}}/A_{\text{cont}}$$

Hydroxyl radical scavenging assay

The ability of *J. insularis* to scavenge OH was determined by the method described by Kunchandy and Rao (1990) 1 ml of the assay mixture (containing 100 µl of 2-deoxy-D-ribose, 500 µl of the extract, 200 µl EDTA and 200 µl of FeCl₃, 100 µl of H₂O₂ and 100 µl of ascorbic acid), was incubated at 37°C for 1 h. 1 ml of thiobarbituric acid and 1 ml of trichloroacetic acid were added to the mixture after an hour of incubation and incubated again at 100°C for 20 min. After cooling, absorbance was taken at 532 nm against a blank sample. Gallic acid was used as positive control.

Scavenging of hydrogen peroxide

The ability of *J. insularis* to scavenge H₂O₂ was determined according to the method of Ruch (Ruch et al., 1989). A solution of H₂O₂ (40 mM) was prepared in phosphate buffer (pH 7.4) and the concentration of H₂O₂ was determined spectrophotometrically by measuring the absorbance at 230 nm. Ascorbic acid was used as positive control.

RESULTS AND DISCUSSION

Proximate composition

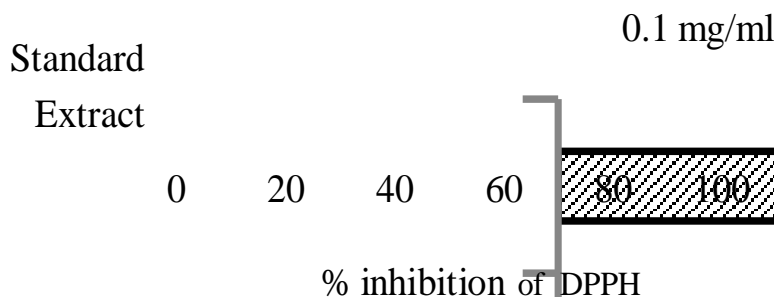
The results of proximate composition of *J. insularis* are presented in Table 1. The results revealed high ash content (15.955%) when compared to that reported in ten green leafy vegetables in South-Western Nigeria (0.2 to 3.9 g/100 g) (Olaiya and Adebisi, 2010). High ash content indicates the level of the mineral deposit in the plant materials. From the result, the value of fat was observed to be 2.144%. This value is similar to percentage fat reported in ten green leafy vegetables in South-Western Nigeria. The low value of fat recorded showed that *J. insularis* can be recommended as a weight reducing diet since low fat food reduces the level of cholesterol and obesity (Gordon and Kessel, 2002). The protein content of the sample (4.48%) was found to be similar to values observed in ten green leafy vegetables in South-Western Nigeria. Although *J. insularis* have low protein concentration it can still serve as a source of protein considering the level of protein deficiency in the society. The energy value (18.367 MJ/kg) obtained was lower than some common green vegetables in South-Western Nigeria (Gordon and Kessel, 2002). The results of the proximate analysis revealed that *J. insularis* is nutritious when compared to other vegetables consumed in Nigeria.

Table 1. Proximate composition of *Justicia insularis*.

Parameter	Concentration percent
Ash	15.955
Protein	4.48
Fat	2.144
Energy	18.367 MJ/kg

Table 2. Mineral composition of *Justicia insularis*.

Element	Concentration percent
Calcium	3.30
Magnesium	0.76
Potassium	1.68
Phosphorous	0.11
Sodium	631.04 mg/g
Manganese	334.02 mg/g
Iron	4.490.08 mg/g
Copper	6.31 mg/g
Zinc	49.72 mg/g

**Figure 1.** Scavenging activity of ethanol extract.

Mineral composition

The mineral constituents of *J. insularis* are shown in Table 2. The contents of calcium, magnesium, potassium and phosphorus were 3.30, 0.76, 1.68 and 0.11%, respectively. These values, except that of calcium, are low compared to those reported in the ten green leafy vegetables in South-Western Nigeria. The iron, sodium, manganese, and zinc contents of the sample were observed to be very high compared with those reported in the ten green leafy vegetables in South-Western Nigeria. Consequently, the need for supplementary diet rich in K^+ (potassium) and Mg^{2+} (magnesium) to avoid metal deficiency syndrome. Distorted enzymatic activity and poor electrolyte balance of the blood fluid are related to inadequate K^+ and Mg^{2+} and as they among the most required elements of living cells (National research

council, 1993).

2,2-Diphenyl-1-picrylhydrazyl radical (DPPH) radical scavenging activity

The free radical scavenging activity of ethanol extract of *J. insularis* against the standard gallic acid is provided in Figure 1. The *J. insularis* extract gave DPPH scavenging activity (82.1%), which was higher than that obtained for the standard (77.9%). Thus *J. insularis* seem to be a good source of natural antioxidants.

Hydroxyl radical scavenging activity

The results are shown as an inhibition rate in Figure 2. *J.*

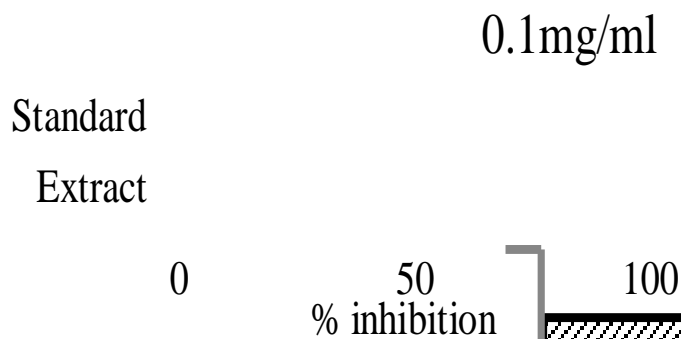


Figure 2. Inhibition rate.

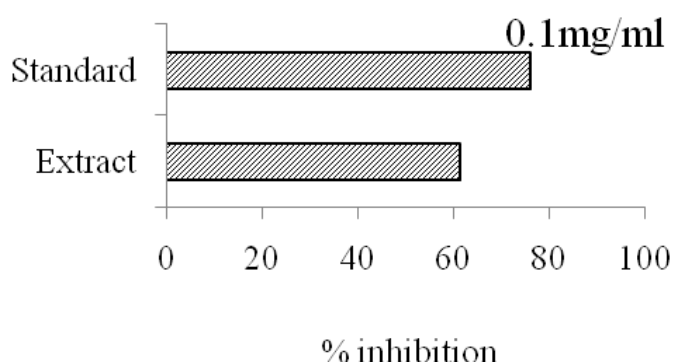


Figure 3. Lower H₂O₂ scavenging activity.

insularis exhibited the lower inhibition of 68.4% but standard gallic acid showed higher inhibition of 75.9%.

Scavenging of hydrogen peroxide

The ability of *J. insularis* to scavenge H₂O₂ was determined according to the method of Ruch et al. (1989). Figure 3 indicates that *J. insularis* exhibits a lower H₂O₂ scavenging activity of 61.5% compare to the standard of ascorbic acid whose scavenging effect is 76.3%.

Conclusion

This study has revealed that *J. insularis* consumed in Southern part of Nigeria can contribute useful amount of mineral elements to human diet. However, the protein and the fat contents of this vegetable are not enough to satisfy the recommended dietary allowances (RDAs) for these macronutrients. Extract from *J. insularis* showed antioxidant properties were similar to antioxidant properties of the standards used. There are few reports on the antioxidant capacity of *J. insularis* and the

mechanism of *J. insularis* as antioxidative agents is still not fully understood. Hence, further research is recommended to analyze and isolate the active compounds responsible for the antioxidant activity from *J. insularis*

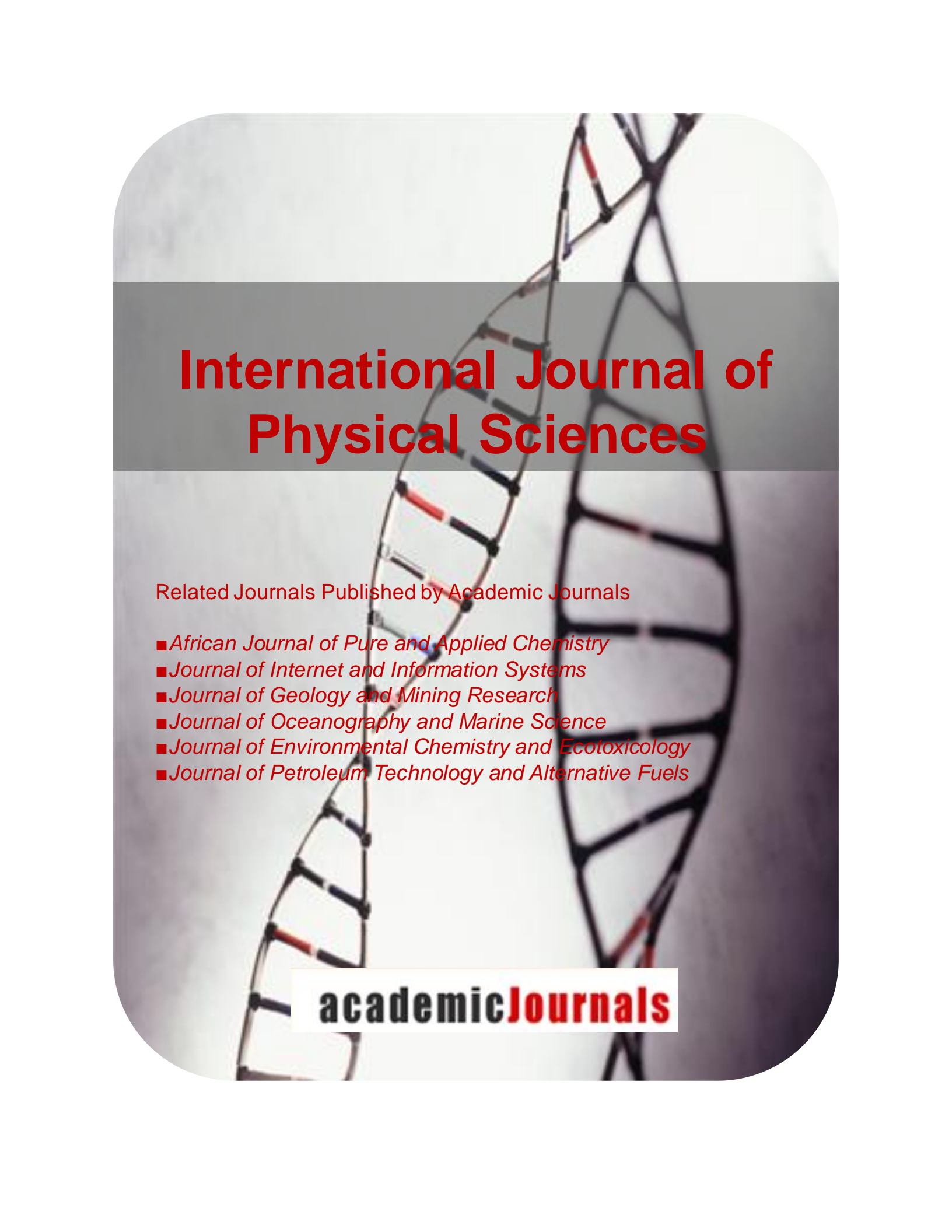
Conflict of Interest

The authors have not declared any conflict of interest.

REFERENCES

- Achu MB, Fokou E, Tchiegang C, Fotso M, Tchouanguep FM (2005). Nutritive value of some *Cucurbitacea* soil seeds from different regions in Cameroon. *Afr. J. Biotechnol.* 4:1329-1334.
- AOAC (1990). Official methods of analysis . Association of Analytical Chemist 15thed Washington DC. 12-13.
- Atasie VN, Akinlanmi TF, Ojiodu CC (2009). Proximate analysis and physico-chemical properties of Groundnut. *Pak. J. Nutr.* 8(2):194-197.
- Blois MS (1958). Antioxidant determinations by the use of a stable free radical. *Nature.* 181:1199-1150
- Enoch A, Margaret P, Franciose A, Ndanikou S, Alexander D, Bianca D (2009). Traditional vegetables in Benin: Diversity, distribution, ecology, agronomy and utilization. Darwin initiative project 15/003 & international foundation of science project T/3701-1. Draft. 94-95.
- Ganthavorn C, Hughes JS (1997). Inhibition of soybean oil oxidation by extracts of dry beans (*Phaseolus vulgaris*). *J. Am. Oil Chem. Soc.* 74: 1025-1030.

- Gordon MN, Kessel MN (2002). *Perspective in nutrition*. McGraw Hill company, Ohio, New York. 5:257-281.
- Hepper K (1965) *Justiciaschimperi* (Hochst.) Danby/striata [family ACANTHACEAE]. Kasamany 443:137-K.10. www.plants.jstor.org/upwta/1_51
- Jitoe A, Masuda T, Tengah IGP, Suprpta DN, Gara IW, Nakatani N (1992). Antioxidant activity of tropical ginger extracts and analysis of the contained curcuminoids. *J. Agric. Food Chem.* 40:1337-1340.
- Kunchandy E, Rao MNA (1990). Oxygen radical scavenging activity of curcumin. *Int. J. Pharm.* 58: 237-240.
- National research council (1993). *Nutrient requirement by warm water fishes*. Washington .D.C. National Academic press.120.
- Nijveldt RJ, van Nood E, Evan H, Boelens DE, van Norren PG, van Leeuwen KPA (2001). Flavonoids: A review of probable mechanisms of action and potential applications. *Am. J. Clin. Nutr.* 74:418-425.
- Olaiya C, Adebisi J (2010). Phyto-evaluation of the nutritional values of ten green leafy vegetables in South -Western Nigeria. *The Internet J. Nutr. Wellness* 9(2):5580/1150.
- Richard AE, Djukwo VN, Gouado I, Mbofung CM (2007). Nutritional component of some non conventional leaf vegetable consumed in Cameroon. *Pak. J. Nutr.* 6(6):712-717.
- Ruch RJ, Cheng SJ, Klaunig JE (1989). Prevention of cytotoxicity and inhibition of intracellular communication by antioxidant catechins isolated from Chinese green tea. *Carcinogen.* 10:1003–1008.
- Vinson JA, Hao JA, Su Y, Zubik XL (1998). Phenol antioxidant quantity and quality in foods and vegetables. *J. Agric. Food Chem.* 46:3630-3634.
- WHF (2005). *World Hunger Facts*, education service. Summit progress report. FAO publication, Rome.
- Zheng W, Wang SY (2001). Antioxidant activity and phenolic compounds in selected herbs. *Agric. Food Chem.* 49:5165-5170.



International Journal of Physical Sciences

Related Journals Published by Academic Journals

- *African Journal of Pure and Applied Chemistry*
- *Journal of Internet and Information Systems*
- *Journal of Geology and Mining Research*
- *Journal of Oceanography and Marine Science*
- *Journal of Environmental Chemistry and Ecotoxicology*
- *Journal of Petroleum Technology and Alternative Fuels*

academicJournals